
Article:

Alghamdi, F., Zeng, H., Boras, G. et al. (2026) Intrinsic GaAs-engineered p-i-n GaAs/GaAs/AlGaAs nanowires for improved-performance solar water splitting. Optics Continuum, 5 (4). pp. 954-966. ISSN: 2578-7519

https://doi.org/10.1364/optcon.588587

OPTICS CONTINUUM

Intrinsic GaAs-engineered p-i-n GaAs/GaAs/AlGaAs nanowires for improved-performance solar water splitting

FAHAD ALGHAMDI,[1,2,7,†] HAOTIAN ZENG,[1,8,†] GIORGOS BORAS,[1] MAHDI ALQAHTANI,[2] ANDREAS KAFIZAS,[3] HUIWEN DENG,[1] HUI JIA,[1] ZIYUE YIN,[1] RAGHAVENDRA JULURI,[4] MINGQING WANG,[5] ESSA ALHARBI,[2] ALI ALANAZI,[2] JIAJING YUAN,[1] CALUM DEAR,[1] JAE-SEONG PARK,[1] ANTON VELYCHKO,[6] MINGCHU TANG,[1] DAVID J. MOWBRAY,[6] ANA M. SANCHEZ,[4] AND HUIYUN LIU[1]

[1] *Department of Electronic and Electrical Engineering, University College London, London WC1E 7JE, UK*
[2] *King Abdulaziz City for Science and Technology, Riyadh 11442, Saudi Arabia*
[3] *Molecular Science Research Hub, Imperial College London, London W12 0BZ, UK*
[4] *Department of Physics, University of Warwick, Coventry CV4 7AL, UK*
[5] *Institute for Materials Discovery, University College London, London WC1E 7JE, UK*
[6] *School of Mathematical and Physical Sciences, The University of Sheffield, Sheffield S3 7RH, UK*
[7] *fahad.alghamdi.21@ucl.ac.uk*
[8] *haotian.zeng@ucl.ac.uk*
[†] These authors contributed equally to this work.

Abstract: We demonstrate that the addition of an intrinsic GaAs shell to form a p-i-n junction with GaAs/GaAs/AlGaAs core/shells nanowire (NW) enhances the photocurrent density by fivefold compared to a conventional p-n junction with GaAs/AlGaAs NW. The GaAs/AlGaAs material system offers distinct advantages due to its strong visible-light absorption, tunable band structure, and compatibility with protective and catalytic overlayers, such as TiO_2, which can enhance surface stability and charge separation. What we believe to be a novel photocathode structure demonstrates a one-sun photocurrent density of 0.542 mA/cm^2 at an applied potential of 0.20 V with respect to the reversible hydrogen electrode (RHE). This work demonstrates the suitability of GaAs/GaAs/AlGaAs p-i-n core/shells NWs for PEC water splitting and their potential for green hydrogen production.

1. Introduction

Photoelectrochemical (PEC) water splitting is a promising approach that enables the direct conversion of sunlight into chemical fuel, providing a cost-effective method for solar energy storage and sustainable hydrogen production [1,2]. In ideal conditions, breaking the bond of one molecule of H_2O to produce H_2 and ½ O_2 results in a free energy change of $\Delta G_o = 237.2$ kJ/mol, with a threshold energy of $\Delta E_o = 1.23$ eV. To drive this process with light requires the absorption of photons with energies greater than 1.23 eV to trigger the two half-reactions governing water splitting. These are: the oxygen evolution reaction (OER) and the hydrogen evolution reaction (HER), at the semiconductor/electrolyte interface inside the PEC cell [3], as described by the following reactions [4]:

$$H_2O \;+\; 2\,(h^+) \;\rightarrow 1/2\;\; O_2 \;+\; 2H^{\,+} \quad \text{(OER)} \tag{1}$$

#588587 https://doi.org/10.1364/OPTCON.588587
Journal © 2026 Received 29 Dec 2025; revised 27 Feb 2026; accepted 12 Mar 2026; published 25 Mar 2026

$$2H^{+} + 2\,(e^{-}) \rightarrow H_2 \quad \text{(HER)} \tag{2}$$

Group III-V semiconductors are ideal candidates for next-generation optoelectronics and PEC applications due to their mainly direct bandgaps and bandgap energies well matched to the solar spectrum [5,6]. Therefore, III-V based photovoltaic (PV) systems are among the most efficient PV technologies and have been investigated as photoelectrodes for green hydrogen production [7,8]. In particular, GaAs, with a direct bandgap of 1.42 eV, has been extensively studied for solar water splitting applications [9], using various material combinations, such as InP/GaAs [10], p-$GaInP_2$/p-n GaAs [11], and GaInP/GaAs [12], with photocurrent densities ranging from 20 to 120 mA/cm^2. In addition, capping the photoelectrode with a protective layer and co-catalyst has been shown to enhance the performance of solar water splitting compared to an uncapped Ref. [13,14]. For example, titanium dioxide (TiO_2) has been utilized to protect III-V photoelectrodes when combined with catalysts [15]. During water splitting, charge carriers are transported to the electrolyte solution via TiO_2 mid-gap states, in this case, a built-in electric field at the interface region between TiO_2 and the co-catalyst is created that promotes charge separation and transportation to the electrolyte [16]. In addition, studies demonstrate that TiO_2 protection layers, together with a layer of highly active catalyst, could enhance photoelectrode stability under harsh pH electrolyte conditions [17].

In contrast to conventional planar-based photoelectrodes, recent advances have identified nanostructured photoelectrodes, particularly those incorporating nanowires (NWs), as promising candidates for PEC solar water splitting [18,19], in part resulting from the ability to fabricate dense vertical arrays [20,21]. It has been demonstrated that the use of a photoelectrode constructed from vertical NWs arrays, which are perpendicular to the substrate, can promote the transport of charge carriers, e-h collection efficiency and electrolyte ions diffusion at the semiconductor/electrolyte interface [22,23]. Further advantages of III-V semiconductor NW arrays for photoelectrode structures include increased surface area and enhanced charge transfer kinetics at the nanowire–electrolyte interface [24]. NW structures have been regarded as a promising landing to improve the performance, but because of multiple challenges, improvements in performance using NWs have rarely been achieved. The number of reported nanowire photocathode systems is quite small compared to planar photocathodes, even in the few systems reported, the performance (photocurrent, efficiency, stability) is not yet at the levels of more established photocathodes or ideal theoretical limits [25]. In addition, the diffusion path length required for the electron-hole pairs to reach the surface of the structure is shorter in the case of NWs because of their small radial dimensions [26]. Zeng et al [27] have utilized GaAs NW arrays grown by MOCVD for water splitting. Here NiO_x was used as a protective layer; when measured under one sun illumination in 0.1 M KOH pH13, photocurrent densities of 0.01 mA/cm^2 and 0.52 mA/cm^2 were measured for bare and protected samples, respectively. Similarly, GaAs NWs were grown on a silicon substrate by Fan Cui et al. [28] and the photocurrent density of 0.598 mA/cm^2 at 0 V vs RHE under AM 1.5G (100 mW/cm^2) in 0.5 M H_2SO_4 electrolyte pH1 was reported. However, solar water splitting using photoelectrodes has so far demonstrated modest performance compared to planar photoelectrodes, probably due to the presence of shunt routes and a higher rate of surface carrier recombination [29].

It has been suggested that modifying the NW design to form a p-i-n junction can improve the overall device performance. For example, compared to p–n junction, the p–i–n junction offers improved long-wavelength response by enabling charge generation deeper within the device [30,31]. This is due to the thick intrinsic layer forming an extended depletion region, which enhances photon absorption and ensures that more of the generated electron–hole pairs contribute to the photocurrent [32,33].

In the present work, we demonstrate the formation of p-i-n NW photocathodes with a 135 nm-thick intrinsic GaAs layer that plays a key role in enhancing device performance. This work establishes III-V p-i-n core/shell NWs as a viable strategy to overcome carrier recombination and stability issues for solar water splitting applications.

2. Experiments

2.1. MBE growth

Self-catalysed GaAs/GaAs/AlGaAs core/shell and GaAs/AlGaAs core/shell NW samples were grown by solid-source molecular beam epitaxy (MBE) on p-type Si(111) substrates using Al and Ga solid sources and As_4 cracker cells. The Si(111) substrates were annealed prior to growth, to remove any contaminants from the surface, at 600 °C for 60 min. The growth was initiated by the formation of Ga-catalyzed GaAs stems via the self-catalyzed vapor–liquid–solid (VLS) mechanism. Subsequently, the Al flux was introduced to enable the growth of Ga-catalyzed AlGaAs NWs, with nominal Al compositions of 30%. The Ga and Al fluxes were calibrated to match the growth rates required for $Al_xGa_{(1-x)}As$ thin films of equivalent composition grown on GaAs(001) substrates. The Ga flux corresponded to a planar growth rate of 0.6 monolayers per second (ML/s), a constant As_4 beam equivalent pressure (BEP) of 2.75×10^{-6} Torr was maintained, corresponding to an As/Ga flux ratio of 15. At the end of growth, a droplet consumption step was performed by maintaining an As overpressure while terminating the Ga flux at a temperature of 510 °C for 10 min to crystallize the remaining Ga droplet. Incomplete droplet consumption under these conditions can lead to residual Ga at the NW tips, resulting in the enlarged and irregular morphologies observed in SEM figure S1 and S2 of the Supplement 1 (SI).

2.2. Device fabrication

A ~15nm-thick TiO_2 layer was deposited directly onto the GaAs/AlGaAs and GaAs/GaAs/AlGaAs NW photoelectrodes as a protective coating using an atomic layer deposition (ALD) reactor with titanium isopropoxide ($Ti[OCH(CH_3)_2]_4$) and water serving as the metal and oxygen precursors, respectively. Titanium isopropoxide (TTIP) was kept at room temperature, while the water was kept at ~ 5 °C. The deposition temperature was maintained at 150 °C. The growth rate of the process was 0.4 Å per cycle. Immediately afterward, an 8 nm thick Ni co-catalyst coating was deposited onto the TiO_2 layer using a Physical Vapor Deposition A306 Metal Box. For the back contact and to form an ohmic contact to collect the electrons/holes generated from the photoelectrode, Ti/Au (40/80 nm) metals were deposited on the back of all samples by thermal evaporation using a Lesker PVD75 sputter coating system. Next, to optimize the ohmic contact, the back contact metals were annealed at 420 °C for 60 s by rapid thermal annealing using a Solaris 150 Rapid Thermal Processing System. Finally, with the aid of a glass microscope slide to support the photoelectrode device, premium adhesive conductive copper tape was applied to the slide. The sample was then mounted onto the tape using silver paste and encapsulated with a high-quality insulating epoxy. A Schematic of the device fabrication workflow is illustrated in Figure S9 of the SI.

2.3. PEC measurements

Photoelectrochemical (PEC) measurements were performed under AM 1.5 G illumination (one sun) using a three-electrode system The GaAs/AlGaAs core/shell NWs photocathode served as the working electrode, a silver/silver chloride (Ag/AgCl) electrode as the reference, and a platinum (Pt) mesh as the counter electrode. All electrodes were immersed in 1 M KOH electrolyte solution (pH 14), and the active area of the photocathode was 0.25 cm^2. A potentiostat was used to perform linear sweep voltammetry (LSV), all LSV measurements were performed at a scan rate of 50 mV/s, and the measured potentials versus Ag/AgCl were converted to the reversible hydrogen electrode (RHE) using the following Nernst equation:

$$V_{RHE} = V_{Ag/AgCl} + (0.059 \times pH) + V^{\circ}_{Ag/AgCl} \tag{3}$$

where: $V_{Ag/AgCl}$ is the potential experimentally measured versus the reference electrode (Ag/AgCl), pH is the power of hydrogen of the electrolyte solution (pH = 14) and $V^{\circ}{}_{Ag/AgCl\ is}$ the standard potential (0.197 V) of Ag/AgCl at room temperature as well as chronoamperometry for stability tests. Incident photon-to-current efficiency (IPCE) measurements were conducted using a two-electrode setup with a monochromatic light source in 1 M KOH (pH 14).

2.4. Characterization

Room-temperature photoluminescence (RTPL) measurements were carried out using a Nanometrics RPM2000 system. The excitation source was a 532 nm laser with a spectrometer slit width of approximately 0.01 mm and a laser power of 17.4 mW. Power-dependent low-temperature photoluminescence (LTPL) measurements were performed using the same setup at 10 K with varying optical densities (OD) of neutral density filters to control the excitation power. The luminescence signal was collected using an InGaAs detector. Raman spectra were acquired using a Renishaw InVia Raman spectrometer with a green excitation laser at a wavelength of 532.4 nm. Scanning electron microscopy (SEM) images and EDX were acquired at the London Centre Technology (LCN) using a Carl Zeiss XB1540 scanning electron microscope equipped with energy dispersive x-ray spectroscopy (EDAX/EDS) powered by Gatan. Scanning Transmission electron microscopy and EDX compositional analysis were carried out using Jeol-2100 and Jeol-ARM electron microscopes operating at an accelerating voltage of 200 kV. GaAs/GaAs/AlGaAs NWs were transferred onto a lacey carbon grid, and the ultramicrotome sections were prepared with a thickness of 50 nm. XRD, HRXRD and rocking curve measurements were performed using a Malvern Panalytical Materials Research Diffractometer (X'Pert^3 MRD XL) with Cu-Kα_1 radiation.

2.5. Simulations

Simulations of the conduction and valence band profiles were performed using **nextnano++** (version 5.5.9.0, nextnano GmbH). The software numerically solves the Schrödinger–Poisson equations to obtain self-consistent energy band diagrams for homostructure and heterostructure semiconductor

3. Results and discussion

The NWs were grown by molecular beam epitaxy (MBE) via the self-catalyzed method on p-type Si(111) substrates. For GaAs/AlGaAs p-n NWs, the growth started with a p-type GaAs core. After the growth of the core, an n-type AlGaAs shell was grown to form the p-n junction. Two devices were then fabricated based on this p-n junction. The first was kept as a reference sample without TiO_2 (protective layer) or Ni (co-catalyst layer). The second device had the same basic junction, but TiO_2 and Ni were deposited as protective and co-catalyst layers, respectively. For the GaAs/GaAs/AlGaAs p-i-n NWs, the growth began with a p-type GaAs core. After the growth of the core, an i-type GaAs shell was grown, followed by an n-type AlGaAs shell to form a p-i-n junction. Finally, TiO_2 and Ni as protective and co-catalyst layers were added. All the NW structures have an average length of ~ 11 µm, with diameters of 280 nm and 290 nm for the p–n junction and the p–i–n junction, respectively.

A schematic of the three different NW photocathode structures is shown in Fig. 1(a), with details also given in Table 1 (for more details, see the device fabrication section). The formation of p-n and p-i-n junctions results in band edge bending of the conduction and valence bands at the interfaces with strongly bent near the heterointerface as shown in Figs. 1(b) and (c) [34,35].

For both protected samples with either a p-n or p-i-n NW photocathode, a TiO_2 layer was used as a protective coating, with nickel (Ni) serving as a co-catalyst. In contrast, the reference sample lacks the TiO_2 and Ni layers. Most of the NWs are vertical with good morphology and uniformity, as observed in the scanning electron microscopy (SEM) images of Figs. 2(a) and 2(b), for the p-n and p-i-n junction, respectively. The NWs tips exhibit enlarged diameters and present irregular morphology due to the consumption of the Ga nucleation droplet [36,37], these are shown at high magnification in Figs. S1 and S2 of the Supplement 1.

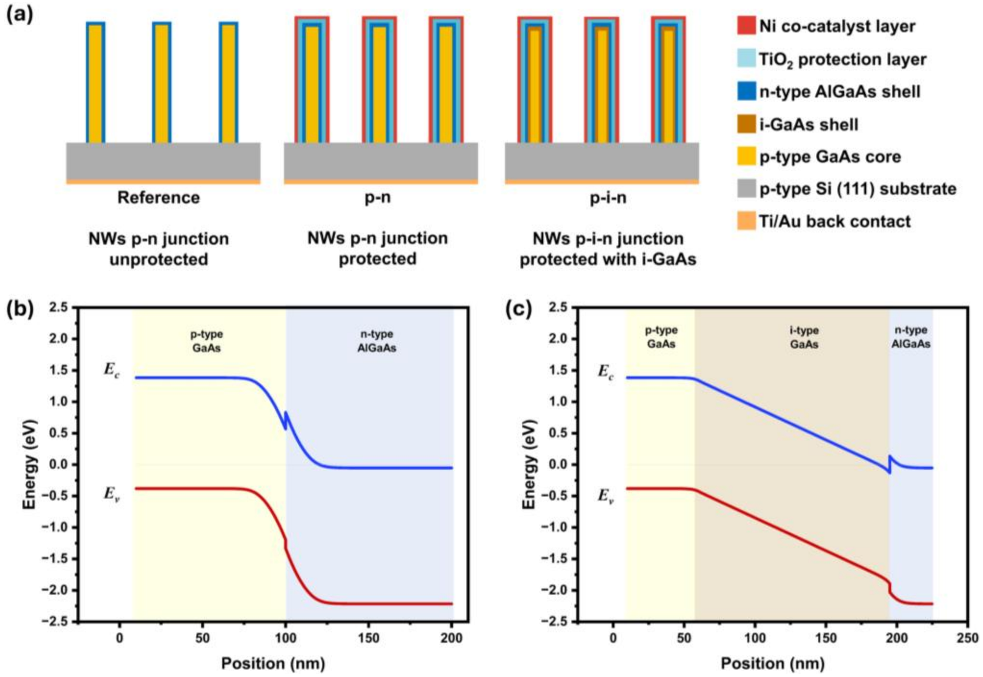

Fig. 1. (a). A schematic showing the fabricated devices: the reference (bare p-n NW photocathode), the p-n NW photocathode (identical to the reference but with a protective layer and co-catalyst), and the p-i-n NW photocathode with an i-GaAs shell and with both protective layer and co-catalyst. (b) and (c) obtained from nextnano simulations shows the energy band diagrams at the interfaces between p-GaAs, and n-AlGaAs for p-n junction and between p-GaAs, i-GaAs and n-AlGaAs for p-i-n junction.

Table 1. Photocathode type, NW structure, and layer details.

Photocathode name	NWs structure	Protection layer	Co-catalyst layer	Back contact
reference	p-n junction	N/A	N/A	Ti/Au
p-n	p-n junction	TiO_2	Ni	Ti/Au
p-i-n	p-i-n junction	TiO_2	Ni	Ti/Au

The optical properties of the NW samples were studied using photoluminescence spectroscopy (PL) at room temperature, as shown in Fig. 2(c). The PL emission peaks at energies of 1.42 and 1.41 eV for the p-i-n and p-n NWs, respectively. The full width at half maximum (FWHM) of the p-i-n sample (20 meV) is narrower, showing higher uniformity, compared to the FWHM of the p-n sample (33 meV) [38]. Further investigation of the optical properties in the intrinsic shell was carried out using excitation power dependent PL at a low temperature of 10 K, as shown in

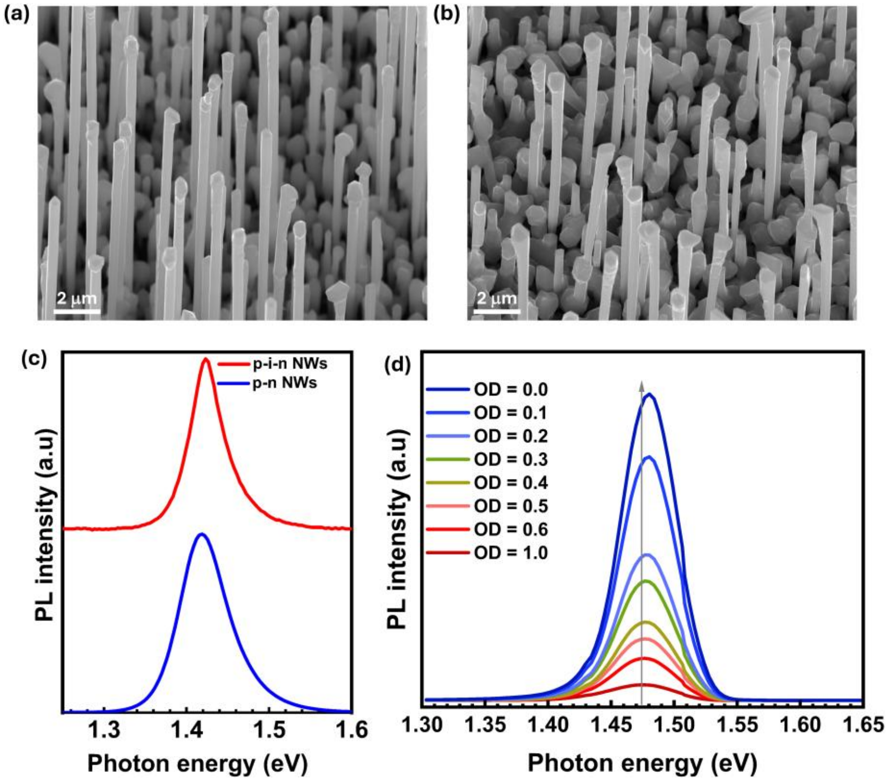

Fig. 2. (a) SEM image of the p-n NWs. (b) SEM image of the p-i-n NWs. (c) PL at room temperature of the p-n NWs and p-i-n NWs. (d) Excitation power dependent PL at 10 K for the p-i-n NWs, where the optical density (OD) of the neutral density filters used in the beam path of the exciting laser are shown in the legend of the figure.

Fig. 2(d). As the excitation power PL increases, the intensity of the emission increases and the emission shifts to higher energy, as a result of band filling [39].

The crystal quality and composition of the NWs and p-i-n photocathodes were investigated by the transmission electron microscopy (STEM) and annular dark field (ADF-STEM) imaging. An image of a representative p-i-n NW is shown in the upper left of Fig. 3. The i-GaAs shell, with a thickness of 135 nm, between the p-type core and the n-type AlGaAs shell is indicated by the white arrow. Energy dispersive x-ray (EDX) mapping was performed with results presented in the remaining images of Fig. 3. The maps corresponding to Al, Ga, As, Ti and O are shown in yellow, blue, purple, orange and green, respectively. It was not possible to produce a clear map visualization of the nickel distribution because of the ultra-thin of this layer. SEM-EDX and EDX line scans are shown in Figs. S3 and S4 of the Supplement 1, respectively.

The crystalline structure of the structures and phases of the TiO_2 and Ni was investigated via XRD 2theta - omega scans using Cu-Kα_1 radiation. Figure 4(a) shows the XRD patterns of the three structures. The lowest angle diffraction peak occurs at a 2θ of 27.26° and results from GaAs (111) and AlGaAs (111) diffraction, the two separate peaks are partially overlapping. A second peak is observed at a 2θ of 28.42° and results from diffraction by the Si (111) substrate. The third peak is observed at a 2θ of 90.13° and is attributed to AlGaAs (333) diffraction, in good agreement with previous studies [40]. To investigate the structural quality of the NWs, rocking curves using omega - 2theta scans were performed and are shown in Fig. 4(b). The presence of

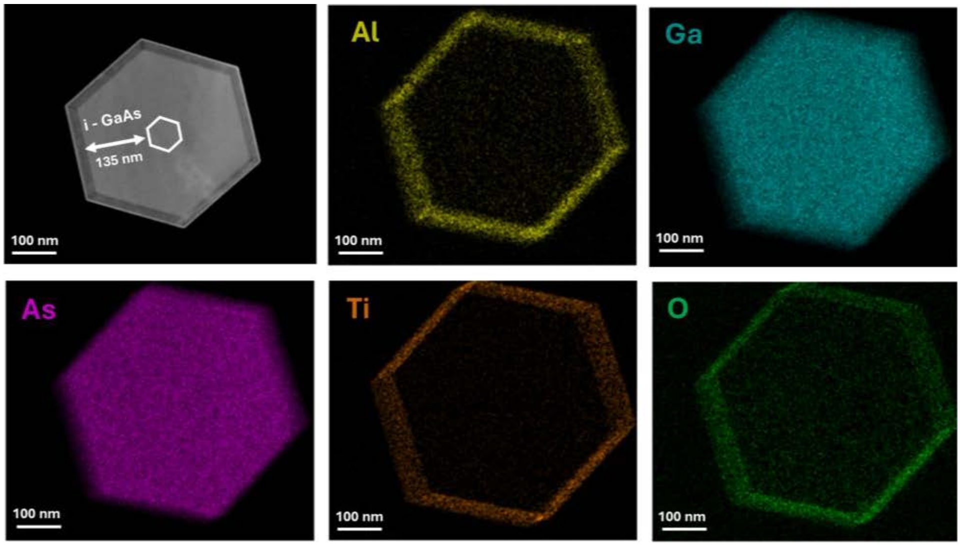

Fig. 3. ADF-TEM image of the ultramicrotome sectioned p-i-n NW photocathode and EDX mapping revealing the elemental distributions.

very narrow FWHMs, 0.018° and 0.024° for both the NWs and substrate, indicates that the NWs have excellent crystallinity and Si wafer used as a substrate is of high quality [41].

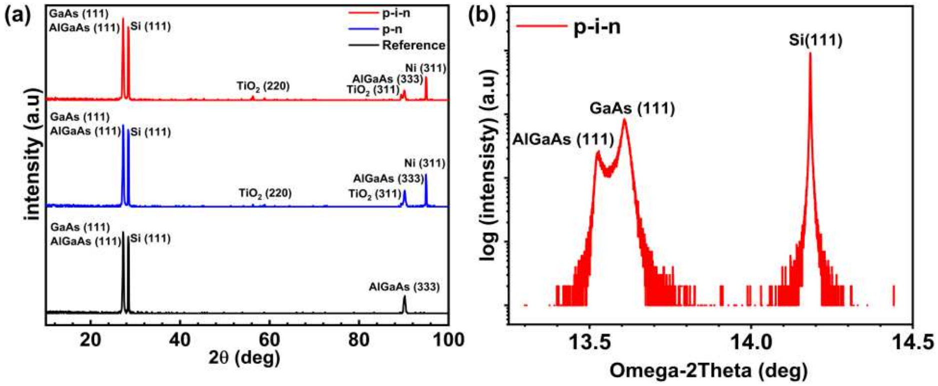

Fig. 4. (a) XRD scans for the three NW photocathode structures, the lowest angle peak at 27.26° is from GaAs (111) and AlGaAs (111) diffraction which are very close to each other and partly overlapping. (b) Rocking curves for the p-i-n NWs and Si substrate demonstrate their high crystallinity.

The PEC performance of the reference, p-n, and p-i-n NWs photocathodes was evaluated using a three-electrode setup under both simulated sunlight (one sun) and in the dark. Figure 5 illustrates the PEC cell setup with the p-i-n NW photocathode present. The photocathode serves as the working electrode, the Ag/AgCl electrode acts as a reference, and a platinum (Pt) mesh as the counter electrode, where the reference electrode measures and controls the potential of the working electrode precisely which improves accuracy in photoelectrochemical measurements compared to the two-electrode setup. All electrodes are submerged in an electrolyte solution of 1 M KOH with a pH of 14.

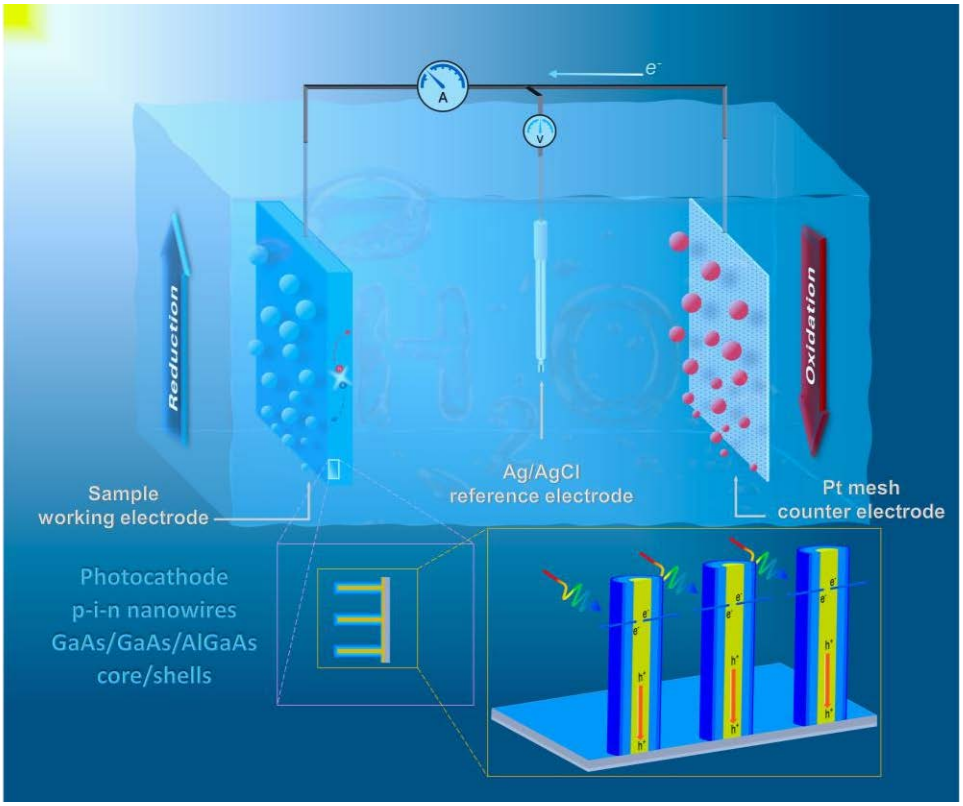

Fig. 5. A schematic diagram showing the three-electrode PEC cell. From left to the right: working electrode (sample), reference electrode (Ag/AgCl) and counter electrode (Pt mesh). The lower figure illustrates the electron-hole pairs generated after the NWs photocathode absorbed photons.

Reduction of water and HER occurs on the surface of the NWs where blue spheres in Fig. 5 represent the bubbles of H_2 gas. Oxidation of water and OER occurs on the surface of the Pt mesh where red spheres represent the bubbles of O_2 gas. The schematic diagram at the bottom right shows the p-i-n NWs receiving photons and the generation of electron-hole pairs in the i-GaAs intrinsic shell. Electrons traverse short paths to the surface then transfer to the electrolyte to reduce the water and produce hydrogen. At the same time, holes move through the stem of the NW to the back contact which is connected to the Pt mesh where the oxidation reaction of water takes place to produce oxygen.

To evaluate the performance of the samples, J–V measurements were conducted for the three structures. As shown in Fig. 6(a), the saturated photocurrents of the reference sample and p-n NW photocathodes are 0.088 and 0.115 mA/cm^2 respectively (measured at a potential of 0.20 V with respect to the reversible hydrogen electrode (RHE)). The slight increase in photocurrent for the non-reference structure is attributed to the combined effect of the Ni co-catalyst and the TiO_2 protective layer. In addition, Ti/Au was utilized for the back contact, where Ti was used for adhesion and Au for low resistance ohmic contact. Annealing at 420°C enhances contact while preventing problems caused by high temperatures, such as dopant diffusion and damage of substrate or NW [42]. A significant improvement in photocurrent is observed for the p-i-n NW-based modified photocathode with a value of 0.542 mA/cm^2, a fivefold increase compared to the reference sample. This is attributed to the addition of the intrinsic GaAs shell which improves photon absorption [43]. In a p-i-n NW, the intrinsic shell plays a vital role in the separation of photo-generated carriers. In the present case the thickness of the i-GaAs is 135 nm, which is much smaller than the diffusion lengths of the charge carriers: electron diffusion lengths $\sim 20\,\mu$m to $2\,\mu$m and hole diffusion lengths $< 1.0\,\mu$m, where the diffusion length is defined as the average distance the charge carrier can travel before recombining [44]. In the p-i-n NW, the i-GaAs shell is between the p-GaAs core and n-AlGaAs shell, effectively enlarging the active region where photons can be absorbed and electron–hole pairs can be generated. This intrinsic region allows photons that penetrate deeper into the NW to be absorbed, in contrast to the p-n NW where absorption is primarily limited to the narrower depletion region at the junction. As a result, the i-GaAs layer contributes to the observed enhancement in photocurrent density by improving charge separation and increasing the volume of the NWs contributing to light absorption. In the present study, the beneficial effect of the i-GaAs shell is evident in its ability to enhance the photocurrent density by reducing carrier recombination and providing a shorter carrier transfer distance, of order the radial dimension of the NW, required to reach the photocathode's surface [45]. The onset potentials for the reference, p-n and p-i-n NW photocathodes are 0.44, 0.46 and 0.53 V respectively. This slight cathodic shift is attributed to the improved charge carrier kinetics at the semiconductor/electrolyte interface due to the use of a co-catalyst in p-n and p-i-n NW photocathodes [46].

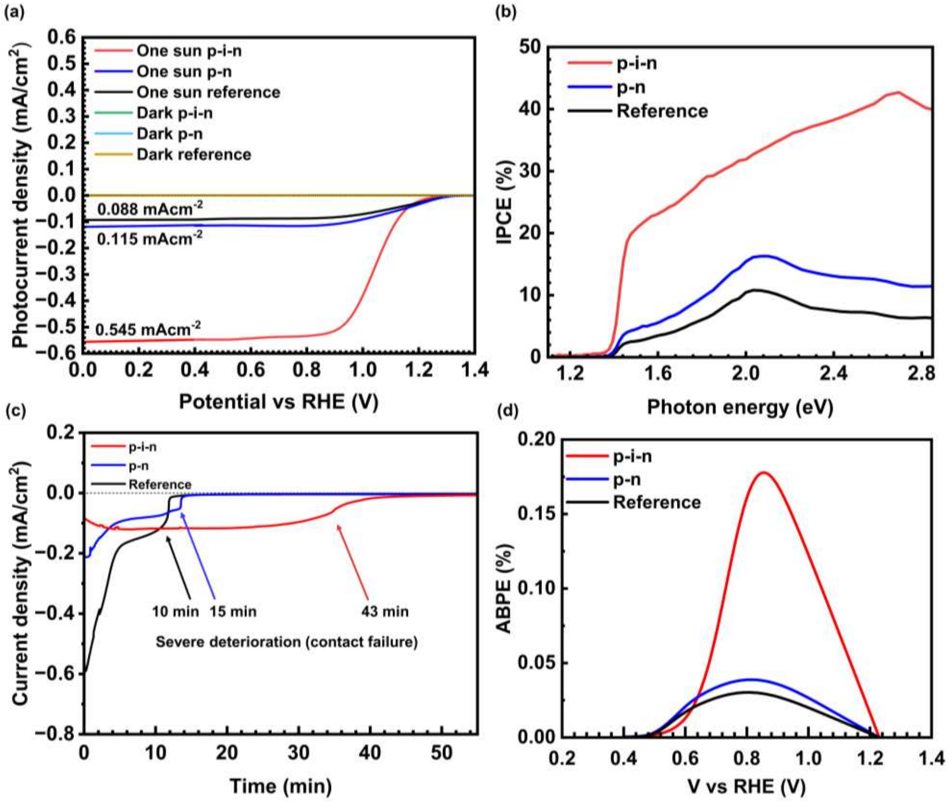

Fig. 6. (a) J-V curves for the three structures. The saturated photocurrent densities of the reference, p-n and p-i-n NW photocathodes are 0.088, 0.115 and 0.545 mA/cm^2 at potential of 0.20 V measured with respect to the reversible hydrogen electrode (RHE), respectively. (b) Plots of the IPCE as a function of wavelength. (c) Stability measurements where the arrows indicate the onset of severe corrosion for each photocathode. (d) Plots of the ABPE as a function of applied voltage.

The incident photon-to-current efficiency (IPCE) quantifies how efficiently the NW photocathode converts incident light (monochromatic photons) into photocurrent (e-h pairs) as a function of photon energy [47], based on equation S1 in the Supplement 1. The IPCE was measured for the three structures using a two-electrode setup at 0 V_{RHE} and 1.0 M KOH with pH14 electrolyte as shown in Fig. 6(b). For the reference photocathode sample, the IPCE shows a lower value in comparison to the p-n and p-i-n NW photocathodes due to the absence of the protective and co-catalyst layers, the highest IPCE for the reference photocathode sample is 11% for a photon energy of 2.07 eV whereas at the same value at 2.07 eV, IPCE shows 16% and 34% for p-n and p-i-n NW photocathodes respectively. The impact of the protective layer TiO_2 and co-catalyst Ni is significant for the p-n photocathode sample where the IPCE is enhanced to 16% at the same photon energy. In general, the two IPCE curves have the same form with an approximately constant enhancement factor for the p-n junction. This enhancement, attributed to the roles of the TiO_2 and Ni, has been previously reported by Maheswari Arunachalam et al [48]. For the p-i-n photocathode sample the IPCE shows a value of ~39% at 2.95 eV, this noticeable enhancement might arise from the contribution of the large band gap of TiO_2 (3.2 eV) [49]. For the p-i-n photocathode a maximum IPCE value of 44% at 2.69 eV is achieved, indicating efficient charge carrier transfer at the semiconductor/electrolyte interface [50]. The IPCE for the p-i-n junction decreases gradually to 20% at 1.48 eV and finally decreases rapidly to below 1% at 1.38 eV. For photon energies below 1.38 eV, the IPCE drops to zero for all three photocathodes because there is no absorption, consistent with the PL results indicating an energy gap of ~1.42 eV.

To assess the corrosion resistance and durability of the NWs photocathodes in electrolyte, a stability test was conducted under one-sun illumination in 1.0 M KOH (pH = 14) for the three structures, as shown in Fig. 6(c). The current density versus time for all samples shows good stability and no contact failure was observed during short-term. However, for longer times, deterioration due to NW degradation in the electrolyte was observed, with contact failure occurring at 10, 14, and 43 minutes for the reference, p–n, and p–i–n NWs photocathodes, respectively. The p-i-n and p-n NWs photocathodes show enhanced stability due to the TiO_2 protective layer and Ni co-catalyst which increase corrosion resistance. The p-i-n NW photocathode shows the best stability, especially in the first ten minutes. This result can be attributed to the greater diameter of the p-i-n NWs, in agreement with a previous study which identified a correlation between the electrode thickness and corrosion rate [51,52].

The dominant degradation pathway for the NW photocathodes is corrosion of the GaAs/AlGaAs NWs in the KOH electrolyte. The reference p–n NW samples without a TiO_2 protective layer degrade more quickly in comparison with the protected samples, where the addition of the TiO_2 protective layer and Ni co-catalyst significantly slows the degradation. Moreover, unlike planar structures, the vertical NW arrays have a high aspect ratio, and ALD of TiO_2 may not fully cover all facets of the NWs. This incomplete coverage can create exposed regions susceptible to electrolyte corrosion, which may explain the observed degradation even in the protected samples. For future improvements, we propose increasing the thickness and optimizing the deposition of TiO_2. Additionally, other wide-bandgap oxides could be employed to provide more robust chemical protection and using a lower-pH electrolyte could also help reduce the corrosion rate as well.

The applied bias photon-to-current efficiency (ABPE) has been reported for photocathode in many photocathode-related studies to represent the performance under an applied voltage [53]. It is calculated from the J–V curve according to equation S2 provided in the Supplement 1. As shown in Fig. 6(d), the ABPE of the p–i–n NWs photocathode reaches to peak at 0.84 V vs. RHE, which is six times higher than the value for the p–n and reference NW photocathode structures. This higher maximum ABPE indicates that the p–i–n NW photocathode exhibits more efficient photocarrier separation and injection than the p–n and reference samples [54].

Despite the inherent advantages of NWs, NW photocathodes - especially radial p–n junctions - often exhibit much lower efficiency than expected. This is largely due to surface recombination, as the high surface-to-volume ratio creates numerous surface states and defects that act as recombination centers, causing photogenerated carriers to recombine before contributing to the current [55]. Moreover, there is a trade-off between absorption and surface effects: while NWs trap light effectively, their large surface exposure increases the number of trap states, so many absorbed photons fail to generate useful current. In addition, the extensive contact area between the NWs and the solution increases corrosion in alkaline electrolyte.

4. Conclusion

To summarize, we have demonstrated the synthesis of a p-i-n NW photocathode structure based on GaAs/GaAs/AlGaAs core/shell NWs with an i-GaAs shell exhibiting improved photocurrent density. The use of TiO_2 and Ni as a protective layer and co-catalyst further enhances the device performance compared to simple p-n NWs photocathode structures measured under the same conditions. The NWs show good uniformity, which indicates high material quality. The p-i-n NW photocathode exhibits a photocurrent density of $0.542\,mA/cm^2$, compared to values of $0.088\,mA/cm^2$ and $0.115\,mA/cm^2$ for the reference and p-n junction respectively, a five-fold increase for the p-i-n junction. In terms of the IPCE, a significant improvement was found for the p-i-n NW photocathode with a value of 44% at 2.69 eV, which indicates efficient charge carrier transfer. In addition, the p-i-n NW photocathode exhibits the best stability inside the electrolyte. Our work demonstrates the suitability of GaAs/GaAs/AlGaAs core/shells NWs for an enhanced performance PEC solar water splitting device and highlights promising potential of this platform for green hydrogen production. Our work can pave the way for wider use of core/shell NW-based photocathodes employing the efficient and mature GaAs/AlGaAs material platform for solar water splitting, thereby contributing to the production of sustainable and ecologically friendly energy.

Funding. Engineering and Physical Sciences Research Council (EP/W002752/1, EP/W002302/1, EP/W002418/1, EP/W017075/1).

Acknowledgment. Fahad Alghamdi, Mahdi Alqahtani, Essa Alharbi and Ali Alanazi gratefully acknowledge the support of King Abdulaziz City for Science and Technology (KACST).

Disclosures. The authors declare no conflicts of interest.

Data availability. Data underlying the results presented in this paper are not publicly available at this time but may be obtained from the authors upon reasonable request.

Supplemental document. See Supplement 1 for supporting content.

References

1. B. A. Pinaud, J. D. Benck, L. C. Seitz, *et al.*, "Technical and economic feasibility of centralized facilities for solar hydrogen production via photocatalysis and photoelectrochemistry," Energy Environ. Sci. **6**(7), 1983–2002 (2013).
2. A. M. K. Fehr, A. Agrawal, F. Mandani, *et al.*, "Integrated halide perovskite photoelectrochemical cells with solar-driven water-splitting efficiency of 20.8%," Nat. Commun. **14**(1), 3797 (2023).
3. M. G. Walter, E. L. Warren, J. R. McKone, *et al.*, "Solar water splitting cells," Chem. Rev. **110**(11), 6446–6473 (2010).
4. A. Fujishima and K. Honda, "Electrochemical photolysis of water at a semiconductor electrode," Nature **238**(5358), 37–38 (1972).
5. X. Wang, M. R. Khan, J. L. Gray, *et al.*, "Design of GaAs solar cells operating close to the Shockley–Queisser limit," IEEE J. Photovoltaics **3**(2), 737–744 (2013).
6. D. E. Aspnes, S. M. Kelso, R. A. Logan, *et al.*, "Optical properties of Al_xGa_{1-x} As," J. Appl. Phys. **60**(2), 754–767 (1986).
7. M. Victoria, N. Haegel, I. M. Peters, *et al.*, "Solar photovoltaics is ready to power a sustainable future," Joule **5**(5), 1041–1056 (2021).
8. S. M. Lee, A. Kwong, D. Jung, *et al.*, "High performance ultrathin GaAs solar cells enabled with heterogeneously integrated dielectric periodic nanostructures," ACS Nano **9**(10), 10356–10365 (2015).

9. D. Kang, J. L. Young, H. Lim, *et al.*, "Printed assemblies of GaAs photoelectrodes with decoupled optical and reactive interfaces for unassisted solar water splitting," Nat. Energy **2**(5), 17043 (2017).
10. R. C. Kainthla, B. Zelenay, and J. O. Bockris, "Significant efficiency increase in self-driven photoelectrochemical cell for water photoelectrolysis," J. Electrochem. Soc. **134**(4), 841–845 (1987).
11. O. Khaselev and J. A. Turner, "A monolithic photovoltaic-photoelectrochemical device for hydrogen production via water splitting," Science **280**(5362), 425–427 (1998).
12. O. Khaselev, A. Bansal, and J. A. Turner, "High-efficiency integrated multijunction photovoltaic/electrolysis systems for hydrogen production," Int. J. Hydrogen Energy **26**(2), 127–132 (2001).
13. S. Cao, Z. Kang, Y. Yu, *et al.*, "Tailored TiO_2 Protection layer enabled efficient and stable microdome structured P-GaAs photoelectrochemical cathodes," Adv. Energy Mater. **10**(9), 1902985 (2020).
14. M. Alqahtani, S. Ben-Jabar, M. Ebaid, *et al.*, "Gallium phosphide photoanode coated with TiO_2 and CoO_x for stable photoelectrochemical water oxidation," Opt. Express **27**(8), A364–A371 (2019).
15. J. Huang, X. Hu, J. Wang, *et al.*, "Unraveling photothermal-enhanced bulk charge transport and surface oxygen reactions in TiO_2 photoanodes for highly efficient photoelectrochemical water oxidation," Chem. Eng. J. **462**, 142246 (2023).
16. S. Lettieri, M. Pavone, A. Fioravanti, *et al.*, "Charge carrier processes and optical properties in TiO_2 and TiO_2-based heterojunction photocatalysts: a review," Materials **14**(7), 1645 (2021).
17. S. Zhao, B. Liu, K. Li, *et al.*, "A silicon photoanode protected with TiO_2/stainless steel bilayer stack for solar seawater splitting," Nat. Commun. **15**(1), 2970 (2024).
18. S. Chandrasekaran, T. Nann, and N. H. Voelcker, "Nanostructured silicon photoelectrodes for solar water electrolysis," Nano Energy **17**, 308–322 (2015).
19. H. Zhang, C. Li, and C. Cheng, "Nanostructured photoelectrodes design for photoelectrochemical water splitting," in *Light, Energy and the Environment 2015*, (Optica Publishing Group, 2015), paper PW3B.5.
20. A. Mukherjee, D. Ren, P.-E. Vullum, *et al.*, "GaAs/AlGaAs nanowire array solar cell grown on Si with ultrahigh power-per-weight ratio," ACS Photonics **8**(8), 2355–2366 (2021).
21. R. R. LaPierre, A. C. E. Chia, S. J. Gibson, *et al.*, "Cover picture: III–V nanowire photovoltaics: review of design for high efficiency," Phys. Status Solidi RRL **7**(10), 815–830 (2013).
22. S. Hoang, S. Guo, N. T. Hahn, *et al.*, "Visible light driven photoelectrochemical water oxidation on nitrogen-modified TiO_2 nanowires," Nano Lett. **12**(1), 26–32 (2012).
23. X. Feng, K. Shankar, O. K. Varghese, *et al.*, "Vertically aligned single crystal TiO2 nanowire arrays grown directly on transparent conducting oxide coated glass: synthesis details and applications," Nano Lett. **8**(11), 3781–3786 (2008).
24. I. Oh, J. Kye, and S. Hwang, "Enhanced photoelectrochemical hydrogen production from silicon nanowire array photocathode," Nano Lett. **12**(1), 298–302 (2012).
25. T. Kirkpatrick, M. J. Burns, and M. J. Naughton, "The effects of geometry on drift-limited solar cells," Phys. Status Solidi B **253**(8), 1653–1659 (2016).
26. E. Garnett and P. Yang, "Light trapping in silicon nanowire solar cells," Nano Lett. **10**(3), 1082–1087 (2010).
27. J. Zeng, X. Xu, V. Parameshwaran, *et al.*, "Photoelectrochemical water oxidation by GaAs nanowire arrays protected with atomic layer deposited NiOx electrocatalysts," J. Electron. Mater. **47**(2), 932–937 (2018).
28. F. Cui, Y. Zhang, H. A. Fonseka, *et al.*, "Robust protection of III–V nanowires in water splitting by a thin compact TiO_2 Layer," ACS Appl. Mater. Interfaces **13**(26), 30950–30958 (2021).
29. V. Andrei, O. Kuehl, and W. A. Smith, "Nanowire photochemical diodes for artificial photosynthesis," Sci. Adv. **9**(6), eade9044 (2023).
30. P. Yu, J. Wu, S. Liu, *et al.*, "Design and fabrication of silicon nanowires towards efficient solar cells," Nano Today **11**(6), 704–737 (2016).
31. J. H. Kim, A. Ma, H. Jung, *et al.*, "In situ growth of the Bi_2S_3 nanowire array on the Bi_2MoO_6 film for an improved photoelectrochemical performance," ACS Omega **4**(17), 17359–17365 (2019).
32. J. T. Wen, Q. L. Chen, and P. Guo, "The thickness and width of the intrinsic region effected electrical properties of GaAs p-i-n photodiodes," Microelectron. Reliab. **151**, 115256 (2023).
33. S. Mokkapati and C. Jagadish, "Review on photonic properties of nanowires for photovoltaics [Invited]," Opt. Express **24**(15), 17345–17358 (2016).
34. K. C. Kao, *Dielectric Phenomena in Solids*, (Academic Press, 2004), chap. 3.
35. S. Al-Janabi, I. Al-Janabi, and N. Al-Janabi, *Analysis the Structural, Electronic and Effect of Light on PIN Photodiode Achievement through SILVACO Software: A Case Study*, (Academic Press, 2023) pp. 165–178.
36. G. Boras, X. Yu, H. A. Fonseka, *et al.*, "Self-catalyzed AlGaAs nanowires and AlGaAs/GaAs nanowire-quantum dots on Si substrates," J. Phys. Chem. C **125**(26), 14338–14347 (2021).
37. Y. Zhang, A. M. Sanchez, Y. Sun, *et al.*, "Influence of droplet size on the growth of self-catalyzed ternary GaAsP nanowires," Nano Lett. **16**(2), 1237–1243 (2016).
38. S. Morkötter, S. Funk, M. Liang, *et al.*, "Role of microstructure on optical properties in high-uniformity $In_{1-x}Ga_xAs$ nanowire arrays: Evidence of a wider wurtzite band gap," Phys. Rev. B **87**(20), 205303 (2013).
39. J.-Y. Huang, L. Shang, S.-F. Ma, *et al.*, "Low temperature photoluminescence study of GaAs defect states," Chin. Phys. B **29**(1), 010703 (2020).
40. C. Moore, "Using photoluminescence to map uniformity," III-Vs Rev. **12**(2), 40–46 (1999).

41. D. Kumar, H. Singh, and S. Banerjee, “Controlled design of phase specific ni nanoparticles from different precursors and their antibacterial activities,” Adv. Sci. Eng. Med. **8**(5), 339–349 (2016).
42. M. M. El-Desoky, I. Morad, M. H. Wasfy, *et al.*, “Synthesis, structural and electrical properties of PVA/TiO_2 nanocomposite films with different TiO_2 phases prepared by Sol–Gel technique,” J. Mater. Sci.: Mater. Electron. **31**(20), 17574–17584 (2020).
43. A. Motayed, J. E. Bonevich, S. Krylyuk, *et al.*, “Correlation between the performance and microstructure of Ti/Al/Ti/Au Ohmic contacts to p-type silicon nanowires,” Nanotechnology **22**(7), 075206 (2011).
44. L. W. Aukerman, M. F. Millea, and M. McColl, “Diffusion lengths of electrons and holes in GaAs,” J. Appl. Phys. **38**(2), 685–690 (1967).
45. I. Benigno and D. Darminto, “Effect of intrinsic layer energy gap and thicknesses optimization on the efficiency of p-i-n amorphous silicon solar cell,” IPTEK J. Sci. **2**(3), a3184 (2017).
46. S. Yamane, N. Kato, S. Kojima, *et al.*, “Efficient solar water splitting with a composite ‘n-Si/p-CuI/n-i-p a-Si/n-p GaP/RuO_2’ semiconductor electrode,” J. Phys. Chem. C **113**(32), 14575–14581 (2009).
47. Z. Chen, T. G. Deutsch, H. N. Dinh, *et al.*, *Incident Photon-to-Current Efficiency and Photocurrent Spectroscopy*, Briefs in Energy (Springer, 2013), pp. 87–97.
48. M. Arunachalam, R. S. Kanase, K. Zhu, *et al.*, “Reliable Bi-functional nickel-phosphate/TiO_2 integration enables stable n-GaAs photoanode for water oxidation under alkaline condition,” Nat. Commun. **14**(1), 5429 (2023).
49. M. Lichterman, B. S. Brunschwig, and N. S. Lewis, “Amorphous TiO_2 coatings stabilize Si, GaAs, and GaP photoanodes for efficient water oxidation,” Science **344**(6187), 1005–1009 (2014).
50. M. Alqahtani, S. Sathasivam, L. Chen, *et al.*, “Photoelectrochemical water oxidation of $GaP_{1-x}Sb_x$ with a direct band gap of 1.65 eV for full spectrum solar energy harvesting,” Sustainable Energy Fuels **3**(7), 1720–1729 (2019).
51. A. S. Altowyan, M. Shaban, K. Abdelkarem, *et al.*, “The influence of electrode thickness on the structure and water splitting performance of iridium oxide nanostructured films,” Nanomaterials **12**(19), 3272 (2022).
52. H. Yin, Y. Wang, L. Ma, *et al.*, “Effect of Surface-Deposited $Ti_3C_2T_x$ MXene on the photoelectrochemical water-oxidation performance of iron-doped titania nanorod array,” Chem. Eng. J. **431**, 134124 (2022).
53. L.-H. Xie, S.-H. Xie, J.-L. Zhang, *et al.*, “Highly efficient hydrogen evolution with silicon nanowire photocathodes: hierarchical triple-junction and a-MoSx catalysts achieving ABPE > 4.6%,” J. Mater. Chem. A **13**(39), 33457–33465 (2025).
54. W. Fang, D. Liu, Y. Zhang, *et al.*, “Improved photoelectrochemical performance by polyoxometalate-modified $CuBi_2O_4$/Mg-$CuBi_2O_4$ homojunction photocathode,” Acta Physico-Chimica Sinica **40**(2), 2304006 (2024).
55. J. Tang, Z. Huo, S. Brittman, *et al.*, “Solution-processed core–shell nanowires for efficient photovoltaic cells,” Nat. Nanotech. **6**(9), 568–572 (2011).